Massive protocluster of a periodic maser source G188.95+0.89

M. M. Mutie [1,2]★ J. O. Chibueze,[3,4]★ K. El Bouchefry [5] G. C. MacLeod,[6,7]★ J. Morgan [3] and P. Baki[1]

[1]*Department of Physics, Technical University of Kenya, P. O. Box 52428-00200, Nairobi, Kenya*
[2]*Department of Physical Sciences, Chuka University, P. O. Box 109-60400, Chuka, Kenya*
[3]*Centre for Space Research, Physics Department, North-West University, Potchefstroom 2520, South Africa*
[4]*Department of Physics and Astronomy, University of Nigeria, Carver Building, 1 University Road, Nsukka, 410001, Nigeria*
[5]*South African Radio Astronomy Observatory, Rosebank, Johannesburg, South Africa*
[6]*The University of Western Ontario, 1151 Richmond Street. London, ON N6A 3K7, Canada*
[7]*Hartebeesthoek Radio Astronomy Observatory, PO Box 443, Krugersdorp 1741, South Africa*

ABSTRACT

We report the results of ongoing monitoring of the 6.7 GHz CH_3OH masers associated with G188.95+0.89. In these observations, five features are periodically varying and at least two exhibit evidence of velocity drifts. It is not clear the cause of these velocity drifts. The spectra have varied significantly since detection in 1991. The $11.45 \, km \, s^{-1}$ feature has decreased exponentially from 2003. Complementary ALMA 1.3-mm continuum and line observational results are also presented. Eight continuum cores (MM1–MM8) were detected in G188.95+0.89. We derived the masses of the detected cores. G188.95+0.89 MM2 was resolved into two continuum cores (separated by 0.1 arcsec) in ALMA band 7 observations. Also, CH_3OH $(4_{(2,2)}\text{-}3_{(1,2)})$ thermal emission associated with MM2 is double peaked. We propose the presence of multiple (at least binary) young stellar objects in MM2. SiO emission exhibits a bow-shock morphology in MM2 while strong emission of ^{12}CO at the east and west of MM2 suggests the presence of an east–west bipolar outflow.

Key words: masers – techniques: interferometric – stars: formation – ISM: individual objects: G188.95+0.89 – ISM: molecules – radio lines:stars.

1 INTRODUCTION

High mass star-forming regions (HMSFRs) is an ongoing topic of open debate as it relates to mass growth (Motte, Bontemps & Louvet 2018). The time-scales of phases associated with this process they state are of the order of 10^4–10^5 yr. Observation of such phases is very difficult. A unique property to HMSFRs is the presence of class II methanol (CH_3OH) masers in their early formative phases (Caswell, Vaile & Ellingsen 1995a; Breen et al. 2013). These class II CH_3OH masers have proven to be a reliable signpost of the very early stages of high-mass star formation (Menten 1991; Caswell 1996). Recent results of monitoring related infra-red sources and class II methanol (CH_3OH) masers towards HMSFRs have identified significant accretion events. At present, only four accretion events have been detected, they are: S255IR-NIRS3 (Fujisawa et al. 2015; Caratti o Garatti et al. 2017; Szymczak et al. 2018b), NGC 6334I (Hunter et al. 2017, 2018; MacLeod et al. 2018), G323.46–0.08 (Proven-Adzri et al. 2019; MacLeod et al. 2021b), and G358.93–0.03 (Breen et al. 2019; MacLeod et al. 2019; MacLeod et al. 2019; Sugiyama et al. 2019; Burns et al. 2020).

Another important phenomena associated with HMSFRs are periodic methanol masers discovered by Goedhart, Gaylard & van

der Walt (2003). Periodic masers are rare, there are only 25 known so far (Goedhart et al. 2003, 2009, 2014; Goedhart, Gaylard & van der Walt 2004; Araya et al. 2010; Szymczak et al. 2011, 2016, 2018a; Fujisawa et al. 2014; Maswanganye et al. 2015; Sugiyama et al. 2015, 2017; Szymczak, Wolak & Bartkiewicz 2015; Maswanganye et al. 2016; Proven-Adzri et al. 2019; Olech et al. 2020). Only the HMSFR source G323.46–0.08 is periodic and has experienced an accretion event (Proven-Adzri et al. 2019; MacLeod et al. 2021b).

The HMSFR G188.95+0.89 (also known as S 252 or AFGL 5180) is well studied at multiple wavelengths. Oh et al. (2010) reported the parallax distance as $1.76 \pm 0.11 \, kpc$, Perseus spiral arm (Reid et al. 2009). The 6.7-GHz CH_3OH masers of this source were discovered by Menten (1991) and reported periodic, $\tau = 395 \pm 8 \, d$, by Goedhart et al. (2004, 2014). Kurtz et al. (2000) report an associated unresolved UCH11 region. Minier et al. (2005) did not detect the continuum radio source, but reported that the masers are projected on a bright mm source with an estimated mass in MM1 of $50 \, M_\odot$. They also detected the presence of CH_3CN and $C^{18}O$ towards the G188.95+0.89 methanol maser site indicating that they are within hot molecular cores (HMCs) with a gas density $\geq 10^5 \, cm^{-3}$.

In this paper, we present the results of ongoing 6.7 GHz CH_3OH maser monitoring for G188.95+0.89. Significant variations of maser features are analysed. Also high-resolution mm-wavelength dust continuum and molecular line emission observations are presented.

★ E-mail: martmulesh@gmail.com (MMM); james.chibueze@nwu.ac.za (JOC); gord@hartrao.ac.za (GCM)

Table 1. Summary of single-dish maser monitoring observations at HartRAO.

Parameter	Quantity
Receiver	4.5 cm
Maser transition	$J = 5_1 - 6_0 A^+$
Rest frequency	6.668518 GHz
System temperature	57 K
Beam width	7 arcmin
Correlator bandwidth	1.0 MHz
Observing mode	Frequency-switching
Number of spectral channels	512
Velocity range	22.5 km s^{-1}
Correlator resolution	0.044 km s^{-1}
Central velocity	+10.0 km s^{-1}
Sensitivity 3σ rms	∼1.0 Jy
Monitoring period	2003 Jun 30–2021 Jan 18
Down time for repairs	2008 Sept–2010 Dec

2 OBSERVATIONS AND DATA REDUCTION

2.1 Single-dish Observations

The radio observations were made using the 26-m telescope of the Hartebeesthoek Radio Astronomy Observatory (HartRAO[1]). The 4.5-cm receiver is comprised of dual, cryogenically cooled, RCP and LCP feeds. Each polarization was calibrated independently relative to Hydra A and 3C 123, assuming the flux scale of Ott et al. (1994).

All observations employed frequency-switching (FS) and within 2 h of zenith. Observations completed with a 1-MHz bandwidth and recorded with a 1024-channel per polarization spectrometer (in FS 512 channels are saved). The velocity resolution achieved is 0.044 km s^{-1} and the typical 3σ root-mean-square (rms) noise per observation was ∼1 Jy. This sensitivity is improved when across several channels, e.g. integration over 10 channels improves the sensitivity to ∼0.3 Jy km s^{-1}. For all the epochs, half-power beam-width pointing correction observations were carried out. The rest frequency was corrected for the Local Standard of Rest (LSR) velocity $v_{LSR} = +10.0$ km s^{-1}. Listed in Table 1 are the parameters of the telescope, receiver, and observation set-up for each epoch.

Observations were made between 2003 June 30 and 2021 January 18 with a cadence of between 10 and 20 d; the cadence varied during several flares. No spectroscopic observations were taken between 2008 September and 2010 December when the 26-m antenna underwent repairs (Gaylard 2010). The position employed at HartRAO is RA = 06^h 08^m 53^{s}3 and Dec. = +21° 38′ 30″ (J2000).

2.2 ALMA Observations

We obtained ALMA band 6 archival data on G188.95+0.89 (Project ID:2015.1.01454.S) taken on 2016 April 23 (42 antennas of the 12-m main array), 2016 September 17 (38 antennas of the 12-m main array). Observations of G188.95+0.89 (phase tracking centre at RA$_{(J2000)}$ = 06^h 08^m 53^{s}3 and Dec.$_{(J2000)}$ = +21° 38′ 30″) were carried out at 1.3 mm (230 GHz) with ALMA band 6 in 2015 using two different configurations. The total time on-source was 19 and 30 min, respectively, and the projected baselines ranged from 15–2600 m. The ALMA correlator was configured to cover nine spectral windows (spws). The raw visibility data were calibrated using the Common Astronomy Software Applications (CASA 5.4)
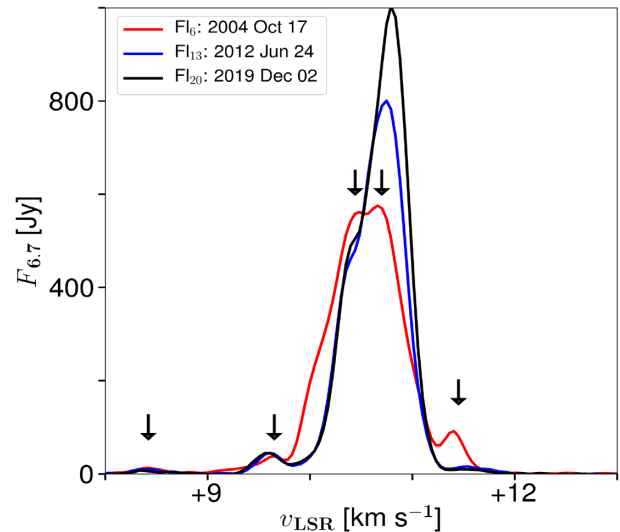
Figure 1. Spectra of the 6.7-GHz methanol masers associated with G188.95+0.89 observed at the maxima of Fl$_6$, Fl$_{13}$, and Fl$_{20}$. Arrows mark the selected velocity features studied here.

standard calibration and imaging tasks. Bandpass and flux calibration were conducted using the sources J0510−1800 and J0750−1231, respectively. J0603−21591 was used as the gain calibrator. The calibrated visibility data from the two observation blocks were combined using CASA task CONCAT, and CLEAN was used to produce the images of the continuum (rms of 2.2 mJy beam^{-1}). Also images of molecular line emission (typical rms of 2.2 mJy beam^{-1}) with spectral resolution of 1 km s^{-1} are produced. In this paper, we will focus on the ^{12}CO (2-1), CH$_3$OH ($4_{(2,2)}$-$3_{(1,2)}$), SiO (5-4), and C^{18}O (2-1). For continuum subtraction, only line-free parts of the spectra were used. We used CASA to do all the calibration and imaging of the data cubes as well as self calibration to remove residual phase and flux calibration errors. The line data were then imaged with a robust weighting of 0.5.

3 RESULTS

3.1 6.7-GHz CH$_3$OH masers variability

In Fig. 1, we present selected spectra from the 17 flare cycles (Fl$_n$ for n = 5 to 21) in the 6.7-GHz methanol maser observations associated with G188.95+0.89 studied here (the original four are published in Goedhart et al. 2004). The spectra presented are the maxima of three of these flare cycles (flare number Fl$_n$ for n = 6, 13, and 20). In this image, it can be seen the evolution of the spectral profile over the 18 yr of observations presented. This profile is certainly comprised of many line blended masers, in particular for $+10 < v_{LSR} < +11.3$ km s^{-1}.

A dynamic spectra is the best way to visualize variability of these 6.7-GHz methanol masers associated with G188.95+0.89, see Fig. 2. Features have weakened others strengthened, most appear periodic and variations in velocity, velocity drifts, are apparent. For the purpose of analysis of these observations five features, two at $v_{LSR} = +10.44$ and $+10.70$ km s^{-1} in the heavily line merged velocity regime, and others at $v_{LSR} = +8.42$, $+9.65$, and $+11.45$ km s^{-1} are selected. Note, the former two features are likely comprised of multiple masers; the others less likely.

Time series plots of the integrated flux density, $F_{Int_{6.7}}$, for each selected feature are shown in Fig. 3. A time series plot of the
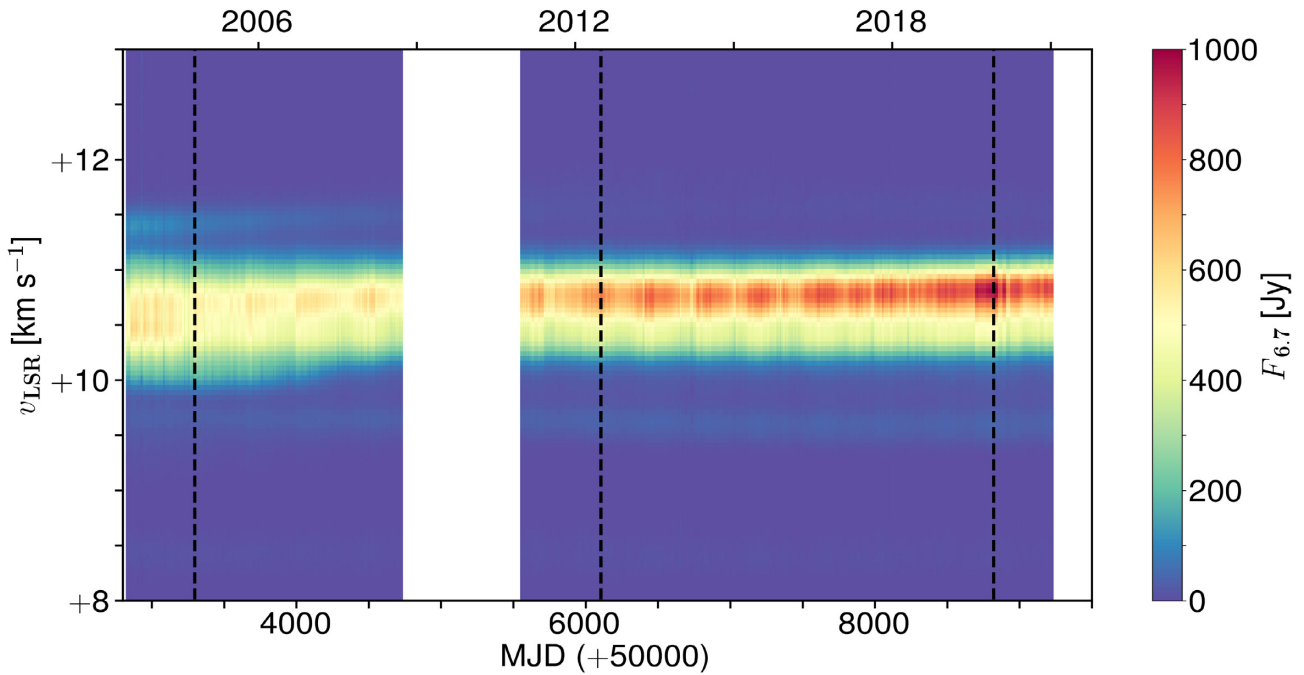
Figure 2. The dynamic spectrum of the 6.7-GHz methanol masers associated with G188.95+0.89. Dashed lines demarcate the spectra of the maximum in Fl$_6$, Fl$_{13}$, and Fl$_{20}$ and plotted in Fig. 1. No observations were taken between 2008 September and 2010 December during repairs.

total integrated flux density, $F_{Int_{6.7}}$(Total), is also shown. For each feature, in each epoch of observation, the velocity associated with the maximum flux density in the stated velocity extent is determined. Linear regression analysis is applied to each velocity time series to determine the velocity drift, and the results are included in this table. Two of the features have measurable velocity drifts, with 'goodness of fit' values $R^2 > 50$ per cent. The apparent drift seen in the $v_{LSR} = +10.70$ km s^{-1} feature (see Fig. 1) may be the result of variations of heavily line merged masers contributing to the feature. The features at $v_{LSR} = +9.65$ and $+11.45$ km s^{-1} are the best fit by a single Gaussian profile each; both possibly devoid of line merged features.

All five features are periodic though it is not obvious for the feature $v_{LSR} = +11.45$ km s^{-1} in Fig. 3. The period of each is determined using, first the programme Period04 developed by Lenz & Breger (2004) and secondly the Lomb–Scargle (LS) periodogram (Scargle 1982). The results are listed in Table 2. The average period for each method is included and are within 3σ standard deviation of each other, $\tau_{Period04} = 395 \pm 1$ d against $\tau_{LS} = 397.6 \pm 0.7$ d.

The $v_{LSR} = +8.42$ km s^{-1} feature is decaying between 2003 and 2021 while the feature $v_{LSR} = +10.70$ km s^{-1} is increasing in this period. The $v_{LSR} = +9.65$ km s^{-1} feature appears flat in Fig. 3, however, its associated flux density of the central velocity channel in the velocity range (not plotted) is rising. When first detected in 1991 (Menten 1991) the $+10.44$ km s^{-1} feature was the brightest feature, here, it is second strongest and is decaying until MJD 5000, thereafter, it is flat or slightly increasing. The increase is possibly caused by contributions from the $+10.70$ km s^{-1} feature. Finally, for $v_{LSR} = +11.45$ km s^{-1}, it is possible to fit an exponentially decaying function to the flux density time series, see Fig. 4. The fitted function is

$$F_{Int_{6.7}} = a \times e^{MJD/b} + c, \qquad (1)$$

where $a = 150 \pm 4$ Jy km s^{-1}, $b = -1380 \pm 20$, and $c = 1.74 \pm 0.05$ Jy km s^{-1}. Goedhart et al. (2004) reported this feature

reached a maximum on 2001 November 12 (MJD 2225), $F_{Int} \sim 45$ Jy km s^{-1}. From equation (1), on MJD 2225, it is estimated $F_{Int} \sim 30$ Jy km s^{-1}. The projected value is significantly lower than the actual value; they are outside estimated errors. The difference in velocity resolution, here it is 0.044 km s^{-1} while in Goedhart et al. (2004), it is 0.056 km s^{-1}, may account for this difference. Line-merged features may also be a factor. Some other features varied linearly and did not require de-trending for analysis. The complex varying feature $v_{LSR} = +10.70$ km s^{-1} will be analysed more elsewhere.

After equation (1) is subtracted from the original time series the remaining residual, also plotted in Fig. 4, reveals its possible periodic nature. Note the slight increase after MJD 7500; possibly resulting from variations in the $V_{LSR} = +10.70$ km s^{-1} feature. The total integrated flux density plotted in Fig. 3 is seen first falling prior to MJD 5000 then rising suggesting the features decaying dominate prior to MJD 5000 thereafter brightening of the $+10.70$ km s^{-1} feature dominates.

The relative amplitude variation of each flare can be determined using R_{amp}:

$$R_{amp} = \frac{F_{max} - F_{min}}{S_{min}} = \frac{F_{max}}{F_{min}} - 1, \qquad (2)$$

where F_{min} and F_{max} are the minimum and maximum flux densities for each flare cycle and each feature. The results of R_{amp} for each velocity feature are included in Table 2. This value ranges from 0.1 to 2.8 for the five features. Note that $R_{amp} \sim 1$ for the $v_{LSR} = +11.45$ km s^{-1} feature; the amplitude is deceasing approximately proportionally during the decay. No phase lags between maser features were found. This may infer that the periodic features are located such that when the cause of variations occur, it affects each nearly simultaneously. There may be lags shorter than our cadence that we cannot measure nor speculate about.
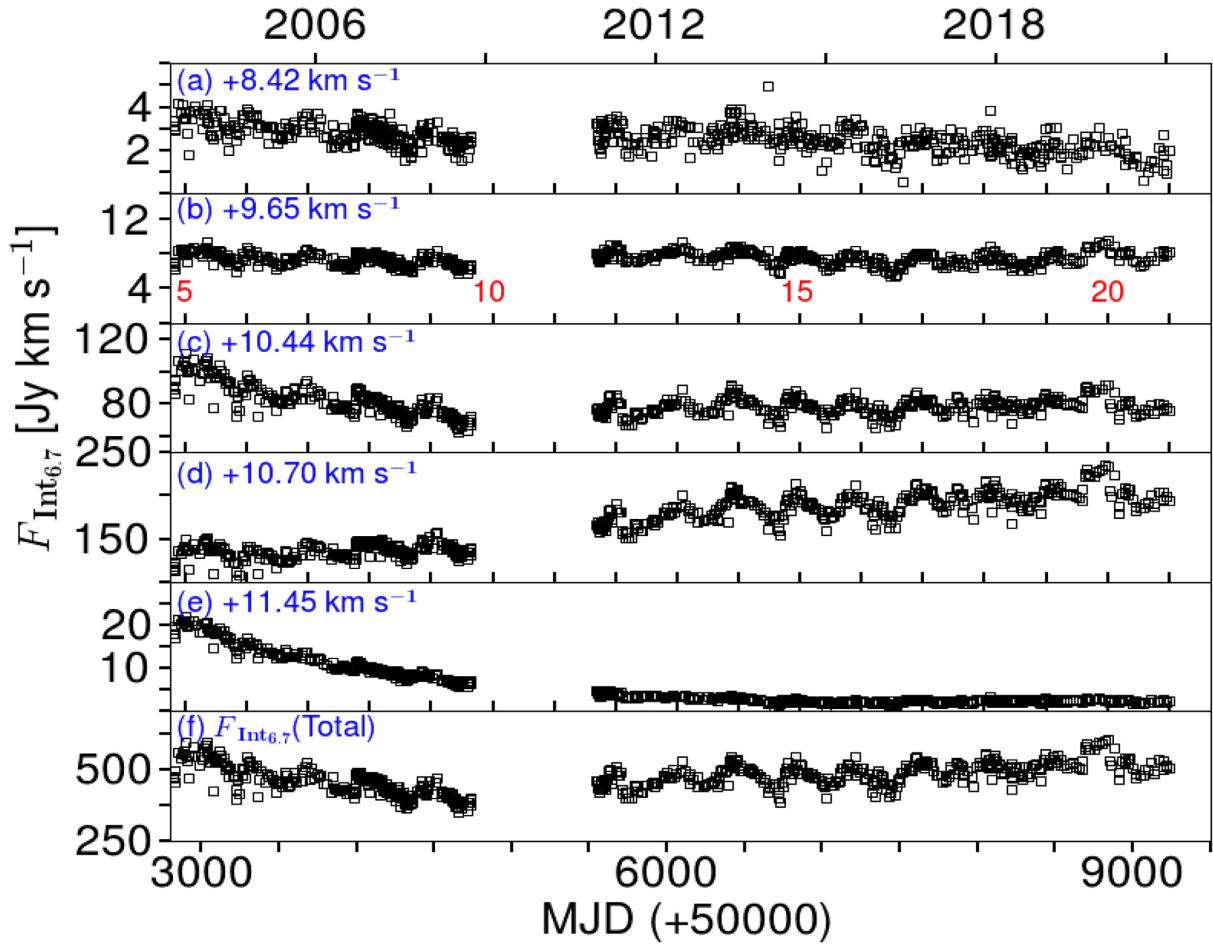
Figure 3. Time series plots of $F_{\text{Int}_{6.7}}$ for five maser features identified in Fig. 1 and labelled in each panel. In (d), the total integrated flux density of all masers associated with G188.95+0.85 is plotted. Note the x-axis in (b) through (e) denote the estimated maxima of each flare, Fl$_n$ for n = 5–21 (for $\tau \sim 395$ d).

Table 2. Information of individual 6.7-GHz maser features. Included are the feature central velocity of each, the velocity extent in which F_{Int} is determined, the velocity drift (1σ standard deviation in parenthesis), its goodness of fit (R^2), the period determined from the Period04, and LS methods, and description of long-term variation. The average period for each method is presented (1σ standard deviation in parenthesis). Comments on velocity drift are given: uncertain ($R^2 < 50\%$), blue-shifting, and red-shifting. Comments on general trends of the flux density of each feature are given (each are periodic).

| Feature | Velocity | | R^2 | Period | | Relative | Comments | |
| | Extent | Drift | | τ_{Period04} | τ_{LS} | Amplitude | Velocity | Flux density |
(km s^{-1})	(km s^{-1})	($\times 10^{-5}$ km s^{-1} d^{-1})	(%)	(d)	(d)			
+8.42	0.48	−1.18(7)	22.9	394.4	397.0	2.8	Uncertain	Slowly decreasing
+9.65	0.26	−2.38(3)	81.6	395.8	396.7	0.6	Blue-shifting	Slowly increasing
+10.44	0.18	+ 0.42(4)	30.4	393.5	398.3	0.1	Uncertain	Complex
+10.70	0.31	+0.39(5)	5.7	396.3	398.2	1.0	Uncertain	Increasing
+11.45	0.31	+1.88(4)	66.0		397.8	∼1	Red-shifting	Exponential decay
Average				395(1)	397.6(7)			

3.2 G188.95+0.89 continuum emission

In Fig. 5 (top panel), we show the composite image of G188.95+0.89 in WISE bands 1 (3.4 μm: red), 2 (4.6 μm: green) and 3 (12 μm: blue), and ALMA 1.3-mm dust continuum emission. The WISE image show a central infrared source (bright in all three bands) corresponding to the 850-μm SCUBA MM1 object, and a green (4.6 μm) dominant object south of the central object

corresponding to the 850-μm SCUBA MM2 object (Minier et al. 2005). G188.95+0.89 is resolved into eight 1.3-mm objects (MM1–MM8) with ALMA. MM1–MM4 and MM5–MM8 objects (Fig. 5, bottom panel) are associated with 850-μm SCUBA MM1 and MM2 objects of Minier et al. (2005), respectively.

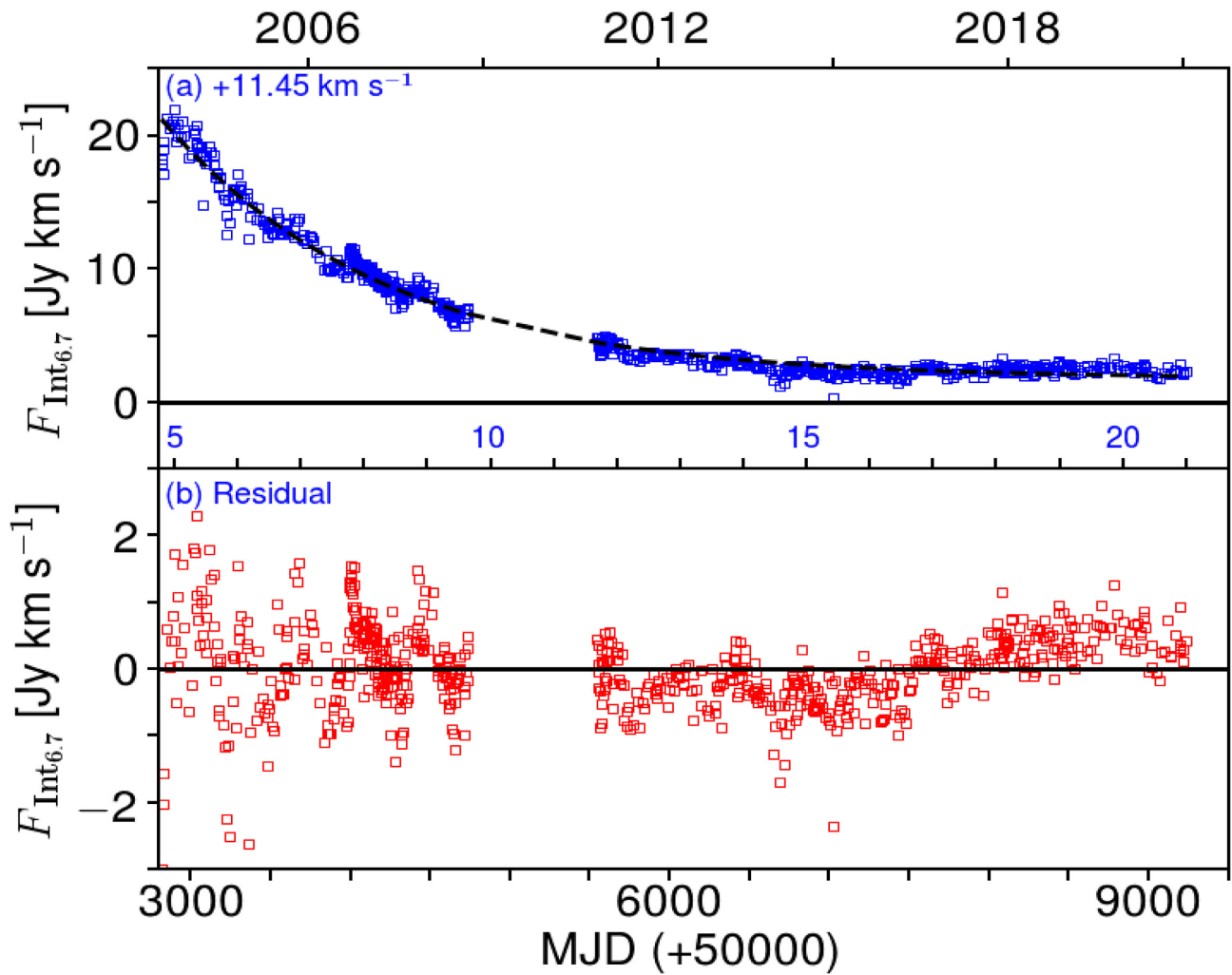ALMA 1.3 mm MM1 and MM2 are central objects (Fig. 5 bottom zoom-in) and MM1 (the brightest dust continuum object)

Figure 4. (a) Time series plot of $F_{Int_{6.7}}$ for the $v_{LSR} = +11.45\,km\,s^{-1}$ feature. The fitted exponentially decaying function (black dashed line) is included. (b) The residual of the integrated flux density, raw data less the fitted exponentially decaying function, is plotted. Note the secondary *x*-axis in (b) denotes the estimated maxima of each flare, Fl_n for n = 5–21 (for $\tau \sim 395\,d$).

is associated with the periodic 6.7-GHz CH$_3$OH maser source. Interestingly, a recent ALMA band 7 observations resolved the continuum core in MM1 into a single object but resolved MM2 into 2 continuum cores (grey contours of Fig. 5 bottom zoom-in). Details of the detected continuum sources and their masses are presented in Table 3.

The dust mass M_d in Table 3, can be estimated by assuming optically thin dust emission using Hildebrand (1983)

$$M_d = \frac{S_\nu\,D^2}{\kappa_\nu\,B_\nu(T_d)} \quad (3)$$

The dust continuum flux density S_ν is given in Table 3 at frequency, ν with D the distance to the source which is 1.76 kpc and κ_ν the dust opacity per unit mass, $\kappa_\nu = 0.33\,cm^2\,g^{-1}$ for 230 GHz (Weingartner & Draine 2001). $B_\nu(T_d)$ is the Planck function at dust temperature, T_d. The temperature used in the dust mass estimations were obtained from Minier et al. (2005), for cores MM1–MM4 a temperature of 42 K is used and for cores MM5–MM8, 50 K is used. To obtain the mass of the cores, a gas-to-dust mass ratio 100 was used and the results are given in Table 3

The integrated flux densities for MM5–MM8, that were also used in the core mass estimates, are not primary beam corrected since MM5–MM8 are located close to the edge of the primary beam and will not be discussed in detail due to limited sensitivity.

3.3 G188.95+0.89 millimeter line emission

A number of thermal molecular lines were detected towards the eight millimeter continuum objects, however in this paper, we will focus only the CH$_3$OH ($4_{(2, 2)} - 3_{(1, 2)}$), SiO ($J = 2 - 1$), ^{12}CO ($J = 2 - 1$), and C^{18}O ($J = 2 - 1$) as shown in Table 4.

3.3.1 CH$_3$OH $4_{(2, 2)}$-$3_{(1, 2)}$

Emission from the CH$_3$OH ($4_{(2, 2)} - 3_{(1, 2)}$) line was detected towards all eight cores, see Fig. 6. The emission is strongest towards the southern MM5–MM8 and weakest towards MM4. The nature of the emission towards MM5–MM8 is contaminated by the effect of the decreased sensitivity towards the edge of the primary beam. Beyond detection or non-detection of an emission, no further discussions will be made for these objects.
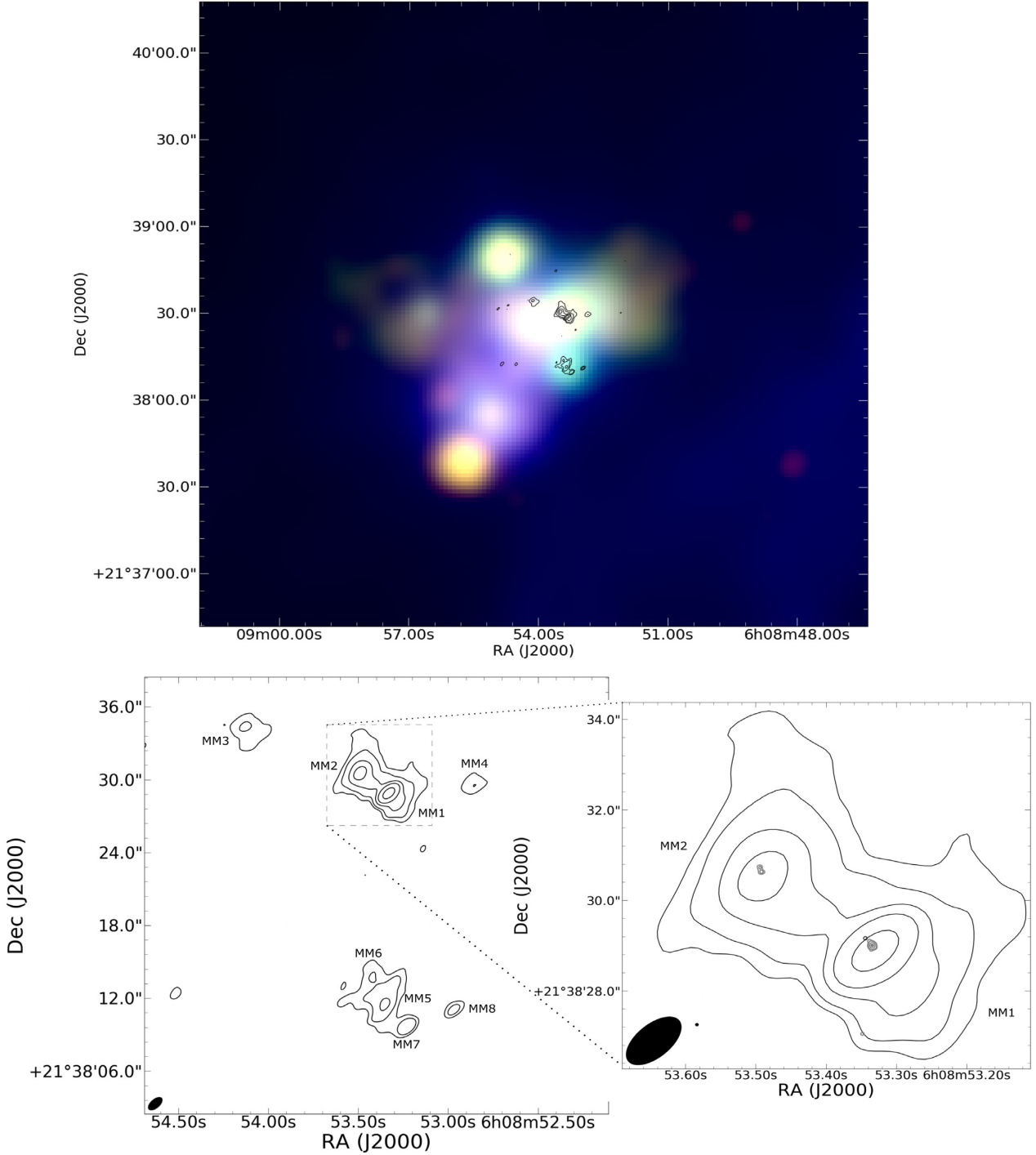
Figure 5. (Top) Composite three-colour WISE image of G188.95+0.89. WISE band 1 (3.4 μm), 2, (4.6 μm), and 3 (12 μm) are represented red, green, and blue. (bottom) ALMA band 6 (black contour, levels = [2, 4, 10, 20, 50] mJy beam^{-1}) and in the zoom-in, band 7 (grey contour, levels = [2, 4, 20, 60, 80] mJy beam^{-1}) dust continuum emission of G188.95+0.89. The filled ellipses on the bottom left-hand corner beams of the band 6 (larger ellipse) and band 7 (smaller ellipse). The open circle near MM1 peak indicates the position of the periodic 6.7-GHz CH$_3$OH masers.

One interesting feature of the CH$_3$OH (4$_{(2, 2)}$-3$_{(1, 2)}$) emission towards MM2 is the presence of a double peak in the emission at the systemic velocity of MM2. There is CH$_3$OH (4$_{(2, 2)}$ − 3$_{(1, 2)}$) emission associated with MM1. Minier et al. (2005) indicated the temperature of the dust of the clump hosting the 1.3 mm ALMA MM1–MM4 sources to be ∼150 K.

3.3.2 SiO (J = 2 − 1)

Emission of SiO (J = 2 − 1) is known to trace shocks especially in star-forming regions. The dominant SiO emission is observed in the north-west region of MM2, see Fig. 7. The emission has a bow-shock morphology in the channel corresponding to the systemic velocity of

Table 3. Parameters of the detected dust cores.

Object-name	RA (h m s)	Dec. (° ′ ″)	Peak flux (mJy beam^{-1})	Integrated flux (mJy)	V_{sys} (km s^{-1})	Core mass (M$_\odot$)
MM1	06 08 53.33	21 38 28.9	71.7	71.1	5.0	8.2
MM2	06 08 53.49	21 38 30.5	22.5	41.3	2.0	4.8
MM3	06 08 54.13	21 38 34.4	5.6	9.4	3.0	1.1
MM4	06 08 52.86	21 38 29.5	3.2	3.8	4.5	0.5
MM5*	06 08 53.35	21 38 11.6	8.3	14.2	2.0	1.4
MM6*	06 08 53.42	21 38 13.7	1.9	3.6	4.0	0.4
MM7*	06 08 53.23	21 38 09.7	9.8	16.7	-	1.6
MM8*	06 08 52.97	21 38 11.1	5.8	6.0	4.0	0.6

Table 4. Parameters of the Observed Lines.

Observed molecular species Molecule	Transition	Rest frequency (GHz)	E_L (K)	E_U (K)
SiO	2-1	217.10498000	20.84	31.26
C^{18}O	2-1	219.56035410	5.27	15.81
CH$_3$OH	$4_{(2, 2)}$-$3_{(1, 2)}$	218.44006300	34.50	45.46
^{12}CO	2-1	230.53800000	5.53	16.60

Note. Columns are species, transition, rest frequency, energy of the upper level, and number of atoms present.

MM2. There are SiO emission (in some cases, very faint emission) associated with each of MM3–MM8, however, no SiO emission is detected towards the MM1 object.

3.3.3 ^{12}CO (J = 2 − 1)

The ^{12}CO ($J = 2 - 1$) emission in G188.95+0.89 is complicated owing to the effect of the strongly self-absorbed features seen in the line emission. The other plausible reason for the observed complex distribution is that all the millimeter objects may be driving outflows. If the strong emission east of MM2 observed in the −3 km s^{-1} channel and the emission west of MM2 in the 9 km s^{-1} channel are both associated with MM2, then they may demarcate an east–west bipolar outflow in MM2, see Fig. 8. There is also some emission north of MM2 and could signify a second outflow emanating from the object; suggestive of multiple YSOs in MM2. The other mm objects are all associated with ^{12}CO ($J = 2 - 1$) emission.

3.3.4 $C^{18}O$ (J = 2 − 1)

We detected high density tracer, C^{18}O ($J = 2 - 1$), towards all MM1–MM8, see Fig. 9. MM1 and MM2 are the dominant sources of the C^{18}O ($J = 2 - 1$) emission. Interestingly, the brightest C^{18}O ($J = 2 - 1$) channel (3 km s^{-1} channel) shows a distribution of the C^{18}O ($J = 2 - 1$) emission to lie in the interface between MM1 and MM2 cores. The possible implication of this to the observed variability in the 6.7-GHz CH$_3$OH masers will be discussed in Section 4.1

4 DISCUSSION

4.1 Implications of the variability in the 6.7-GHz CH$_3$OH Masers

Originally, Goedhart et al. (2004) reported the period of G188.89+0.89 was 416 d; this was revised in Goedhart et al. (2014)

to 395 d. Here, using the longer time series and from two separate methods, the shorter period is confirmed ($\tau_{Period04} = 395 \pm 1$ d and $\tau_{LS} = 397.6 \pm 0.7$ d). Durjasz et al. (2021) also confirm, though observing fewer flare cycles, the shorter period, $\tau = 395 \pm 8$ d.

Class II methanol masers are only found associated with high mass star-forming regions (Minier et al. 2003). Such regions experience accretion events (identified by flaring masers) such as those reported in S255IR-NIRS3 (Fujisawa et al. 2015; Szymczak et al. 2018b), NGC 6334I (MacLeod et al. 2018), G323.46–0.08 (Proven-Adzri et al. 2019; MacLeod et al. 2021b), and G358.93–0.03 (MacLeod et al. 2019; Sugiyama et al. 2019). However, three of the features in Table 2 are decaying, in particular, the $v_{LSR} = + 11.45$ km s^{-1} decays exponentially (Fig. 4). Interesting, historical observations suggest the originally detected peak flux density feature, $v_{LSR} \sim +10.5$ km s^{-1}, has varied markedly since detection, less than 500 Jy before 1993 (Menten 1991; Caswell et al. 1995b), greater than 600 Jy before 2009 (Goedhart et al. 2004; Green et al. 2012) to ∼500 Jy on average here. Note at present the peak flux density is found at $v_{LSR} = + 10.70$ km s^{-1} and not +10.44 km s^{-1}. Caswell et al. (1995b) reported that the feature $v_{LSR} = +11.2$ km s^{-1} decreased slightly from 1991 (∼250; Menten 1991) to 1993 (∼230 Jy). In 1999 August, it was only ∼100 Jy (Szymczak, Hrynek & Kus 2000) while reaching a maximum, ∼160 Jy, in 2001 November (Goedhart et al. 2004); thereafter, the exponential decay is reported here. Above equation (1) cannot describe these variations, nor does it fit the maximum reported in Goedhart et al. (2004). It appears a weak flaring event, increasing by a factor of ∼2.6 in flux density, occurred between 1999 August and 2001 November in the periodic feature at $v_{LSR} = +11.45$ km s^{-1}. This decaying periodic feature resembles that shown for decaying periodic maser features in G323.46−0.08 (MacLeod et al. 2021b). Further analysis of historical data, and data other transitions (e.g. 12.2 GHz CH$_3$OH and/or 22.2 GHz H$_2$O), are required to confirm.

Spot maps of the 6.7-GHz methanol masers are shown in Minier, Booth & Conway (2000) and Hu et al. (2016); all features reside in a 180 × 180 au box assuming a distance of 1.76 kpc (Oh et al.
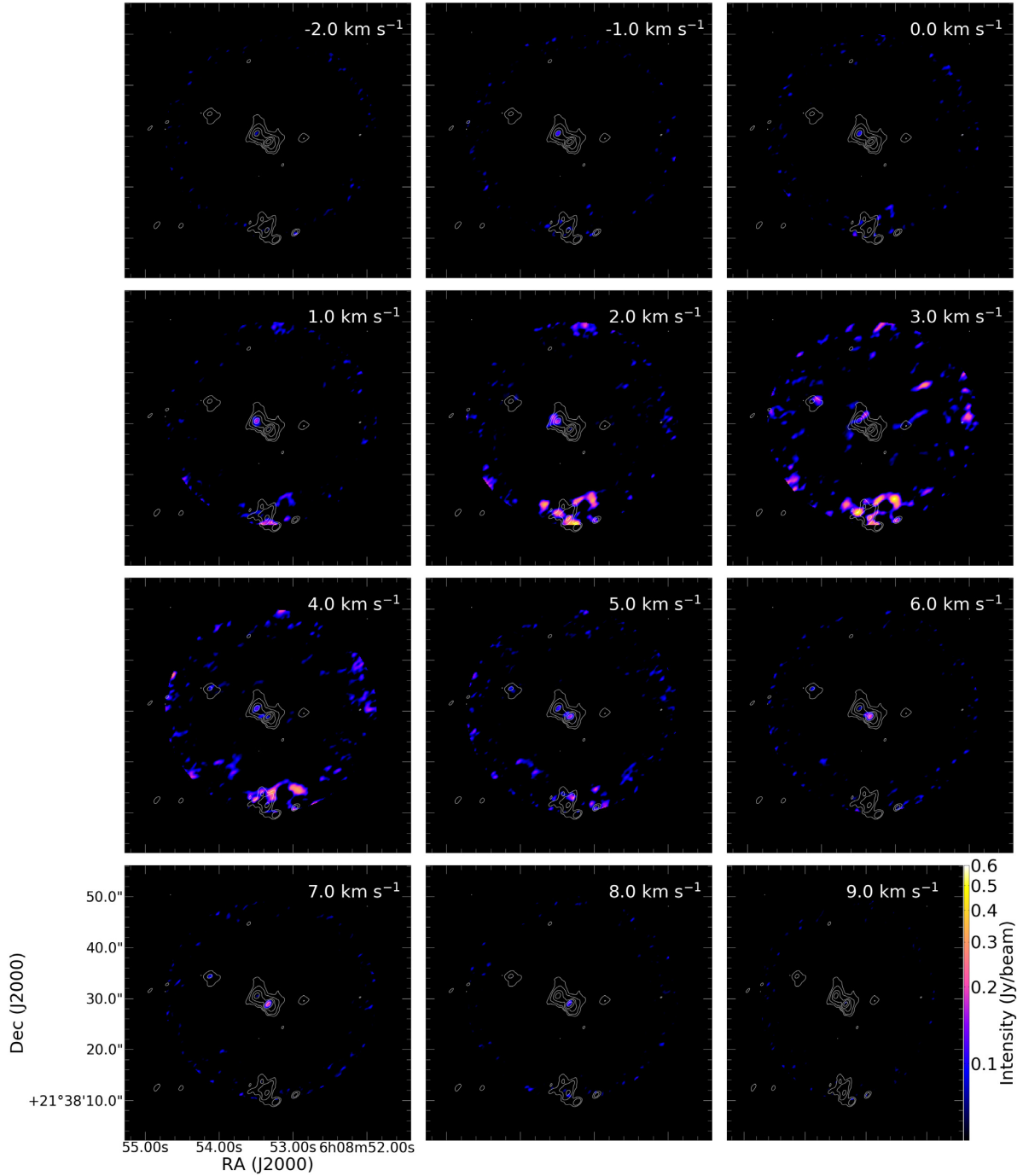
Figure 6. CH$_3$OH 4(2,2)-3(1,2) thermal line channel map with dust continuum overlaid (black contour, levels = [0.002, 0.004, 0.02, 0.06, 0.08] Jy beam^{-1}) dust continuum emission of G188.95+0.89. The colour scale is the intensity in Jy beam^{-1}.

2010) about the bright reference feature (v_{LSR} = + 10.33 km s^{-1}). The weakening features reside within ~50 au radius of the reference feature, v_{LSR} = +8.42 km s^{-1} slightly north while +11.45 km s^{-1} is slightly south of the reference maser. The strengthening feature (+10.70 km s^{-1}) is found ~90 au to the south-east from the reference maser. The non-varying feature, v_{LSR} = + 9.65 km s^{-1}, is further south-east (~140 au). Minier et al. (2000) suggest that the masers surrounding the reference maser could be part of an outflow from the disc.

It is not clear whether velocity drifts, including those seen here, are caused by variability of spectrally blended masers (Szymczak, Wolak & Bartkiewicz 2014) or by motion of the gas (Goddi, Moscadelli & Sanna 2011). The accretion discs surrounding massive star-forming regions may experience infalling gas. Szymczak et al. (2014) report a velocity drifting feature in Cepheus A; they suggest it may be an artefact of variable line-merged features or the result of masers located in regions of infalling gas. MacLeod et al. (2021a) propose the inner radius of the accretion disc surrounding
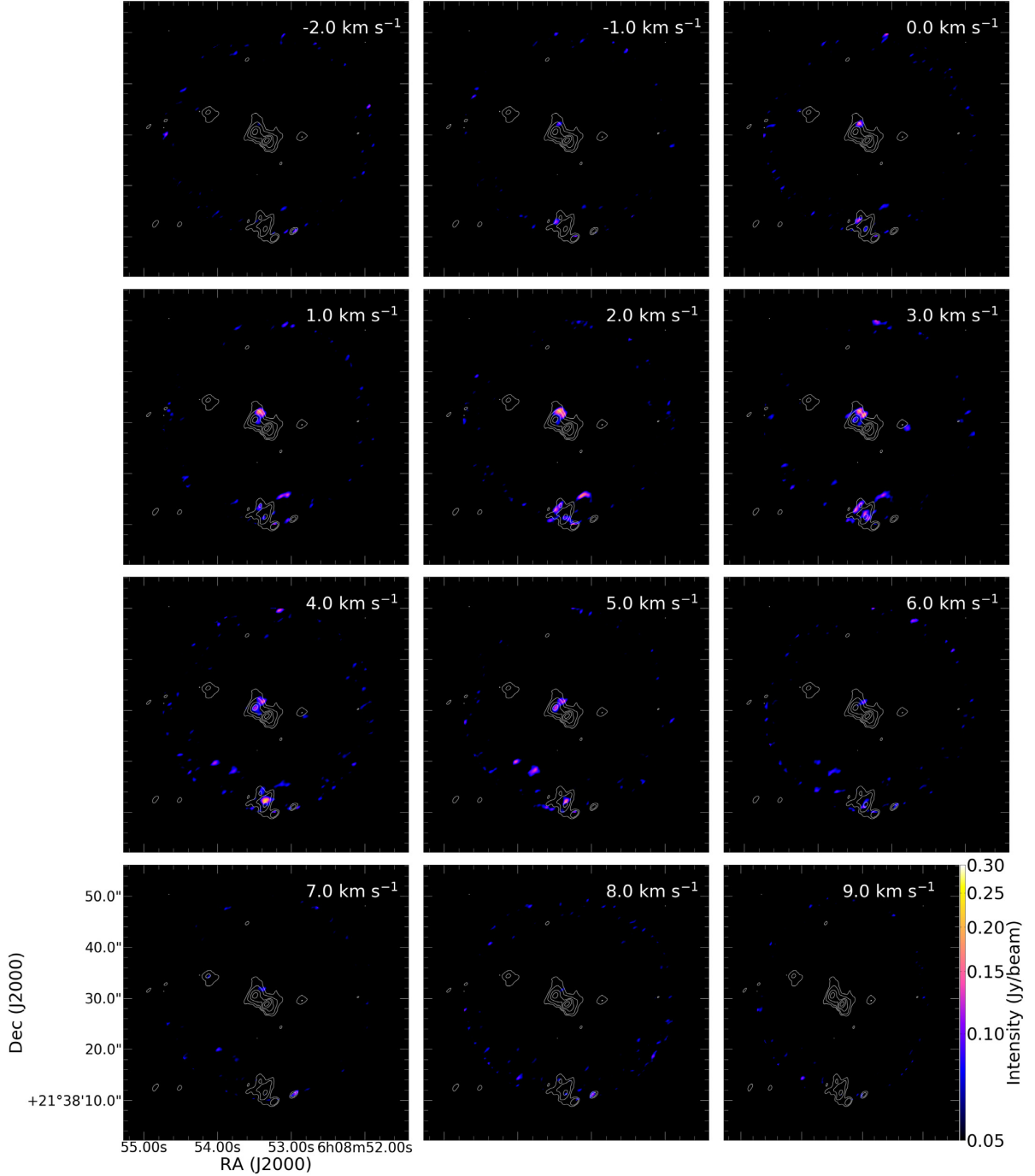
Figure 7. SiO ($J = 2 - 1$) thermal line channel map with dust continuum overlaid (black contour, levels $= [0.002, 0.004, 0.02, 0.06, 0.08]$ Jy beam^{-1}) dust continuum emission of G188.95+0.89. The colour scale is the intensity in Jy beam^{-1}.

the protostar of G9.62+0.20E is infalling resulting in systematic velocity drifts of its associated methanol masers. However, they also state that it may be caused by masers in a precessing disc. Above in Table 2, it can be seen that two features experience measurable velocity drift. The blue-shifted feature, $v_{LSR} = +9.65$ km s^{-1} is blue-shifting ($-2.38 \pm 0.03 \times 10^{-5}$ km s^{-1} d^{-1}) while the other, $v_{LSR} = +11.45$ km s^{-1}, is red-shifting ($+1.88 \pm 0.04 \times 10^{-5}$ km s^{-1} d^{-1}). The drifts are of the order of those seen in G9.62+0.20E (MacLeod et al. 2021a), ranging from

-6 to $+3 \times 10^{-5}$ km s^{-1} d^{-1}. However, an insufficient number of features with measurable velocity drift are found, thus, rendering any comparison to G9.62+0.20E indeterminate. These two features are found well-separated in the spot maps shown in both Minier et al. (2000) and Hu et al. (2016), by ~200 au. Perhaps the central features are influenced by an outflow (Minier et al. 2000) and this motion may force the features at the edges to experience velocity drift. Even the now brightest feature, at $v_{LSR} = +10.70$ km s^{-1}, is blue-shifting though this may be due only to variations of heavily
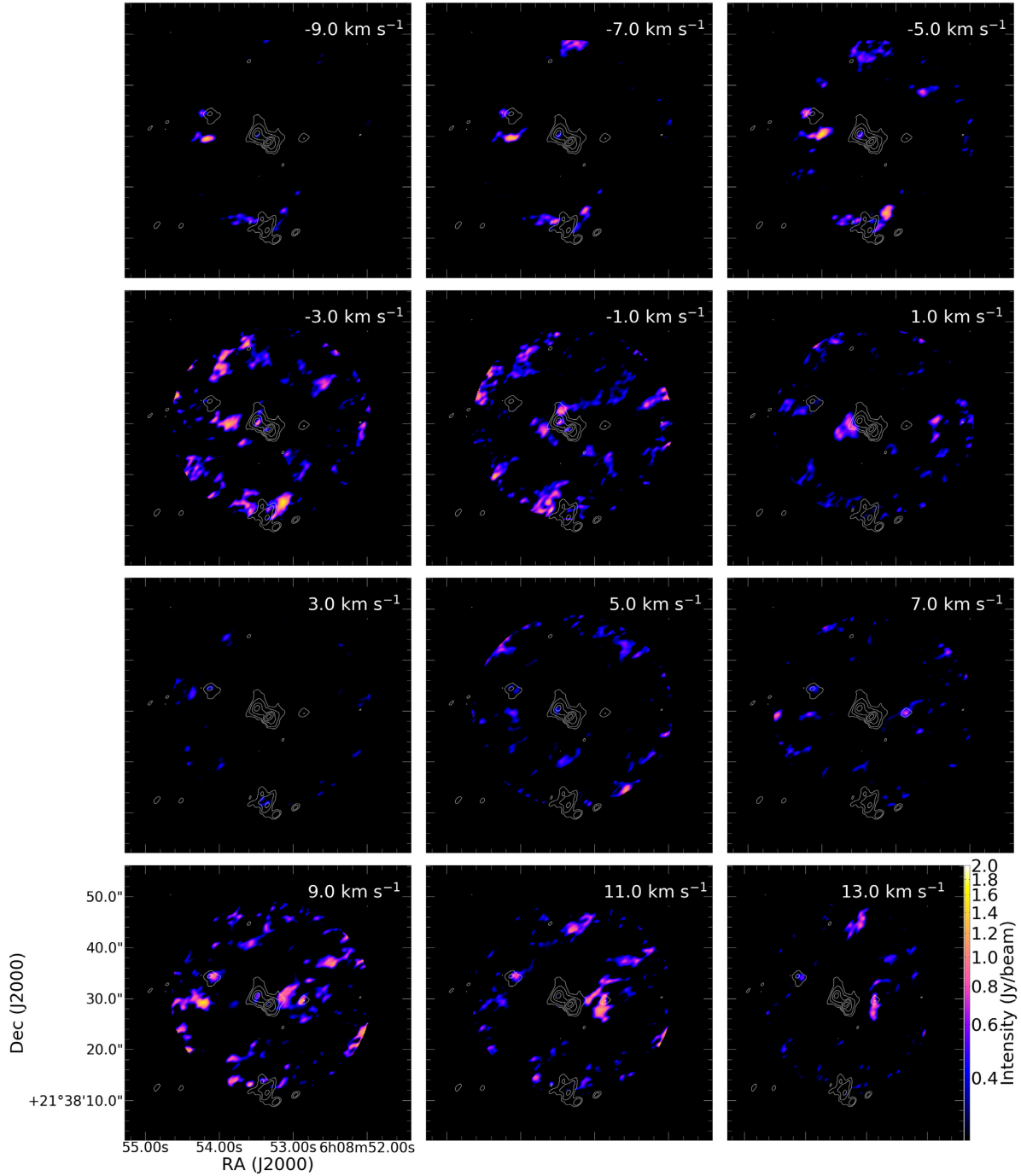
Figure 8. ^{12}CO ($J = 2 - 1$) channel map with dust continuum overlaid (black contour, levels $= [0.002, 0.004, 0.02, 0.06, 0.08]$ Jy beam^{-1}) dust continuum emission of G188.95 + 0.89. The colour scale is the intensity in Jy beam^{-1}.

line-merged features. All of these periodic masers are associated with MM1. More observation and analysis is required to explain these variations.

4.2 Binary system in G188.95+0.89-MM2

There are a number of indicators suggesting the existence of a binary system in MM2. First, the high-resolution ALMA band 7 dust continuum image resolves MM2 into 2 cores separated by 0.1 arcsec. Secondly, the CH$_3$OH ($4_{(2, 2)} - 3_{(1, 2)}$) emission is coincident with

the systemic velocity and the spectral profile of emission towards MM2 has two pronounced features (see 3 km s^{-1} channel of Fig. 6). In Fig. 10, the spectra of ^{12}CO (solid lines) and CH$_3$OH ($4_{(2, 2)} - 3_{(1, 2)}$) (dashed line) taken from MM2 using a 4 arcsec ellipse are presented. It is important to note that the ^{12}CO emission is optically thick. In the ^{12}CO spectra (at least), self-absorption features are visible, implying the ^{12}CO emission is absorbed by cold foreground material in the region. The three vertical dotted lines in Fig. 10 indicate the prominent absorption feature (middle line at 3 km s^{-1}) and two absorption features (-2 and 7 km s^{-1}) one on each side of the
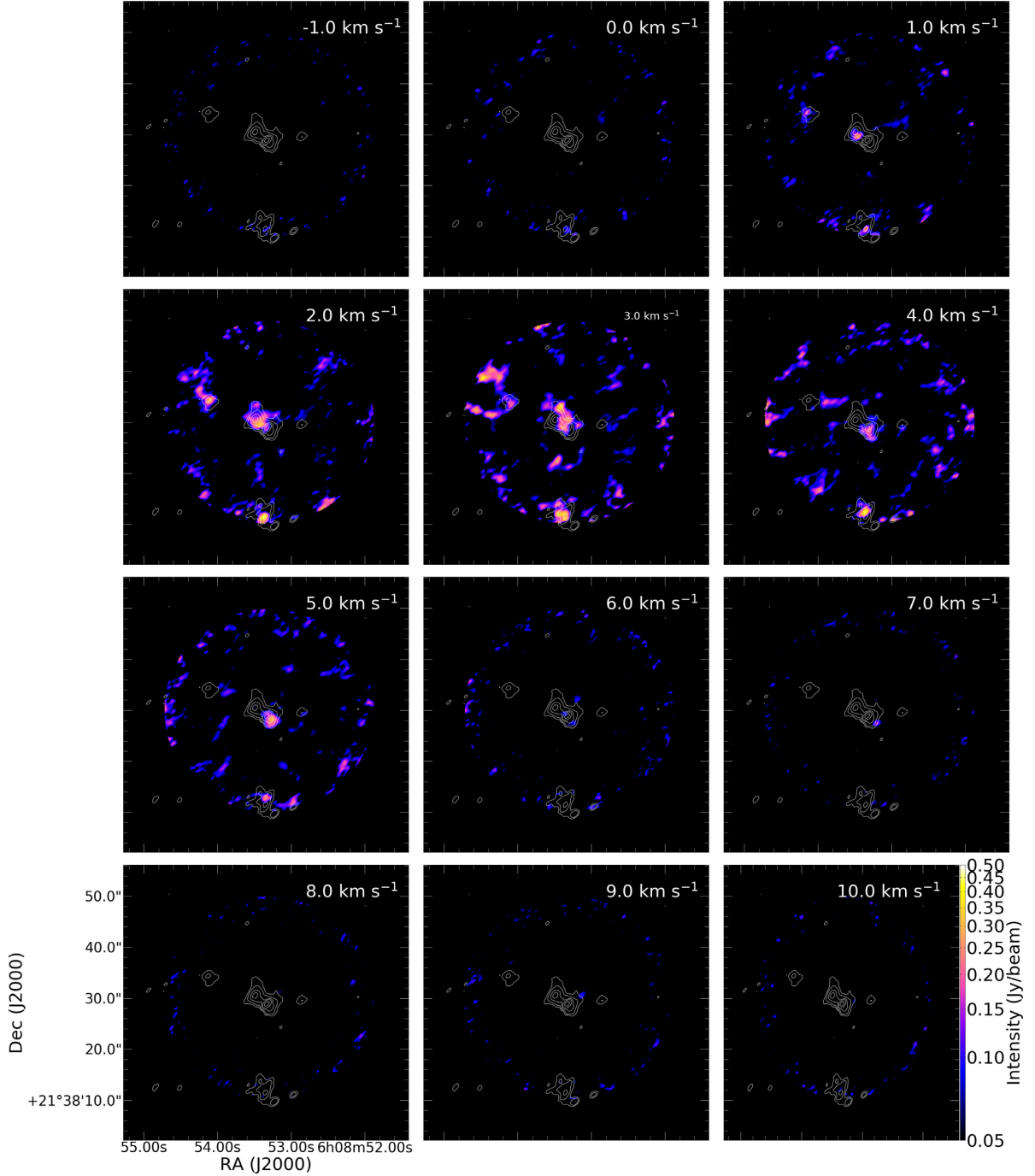
Figure 9. $C^{18}O$ ($J = 2 - 1$) channel map with dust continuum overlaid (black contour, levels $= [0.002, 0.004, 0.02, 0.06, 0.08]$ Jy beam^{-1}) dust continuum emission of G188.95+0.89. The colour scale is the intensity in Jy beam^{-1}.

prominent feature. We noted that missing flux issue can give rise to such spectral feature but in this case, the observed absorption feature is real. The most prominent absorption feature in the ^{12}CO spectra corresponds in V_{LSR} with the CH_3OH ($4_{(2,2)} - 3_{(1,2)}$) absorption feature separating the two resolved cores in MM2. All these observed features suggest multiple (or at least binary) young stellar objects in MM2.

Our suggestion of the presence of at least a binary, or multiple, YSOs in MM2 is supported by the complexity of the orientation of the outflowing gas traced by ^{12}CO, see Fig. 8. An east–west outflow feature with an axis through the peak position of MM2, as well as a

north-west and south-east outflow also intersecting with MM2, can be observed. These support the suggestion at least a binary system is present in MM2. High-resolution continuum and line observations will be required test the multiplicity of YSOs in MM2.

5 CONCLUSION

We presented results of 1.5 decades of monitoring observations of 6.7-GHz CH_3OH masers towards G188.95+0.89 and ALMA band 6 observational results and found the following:
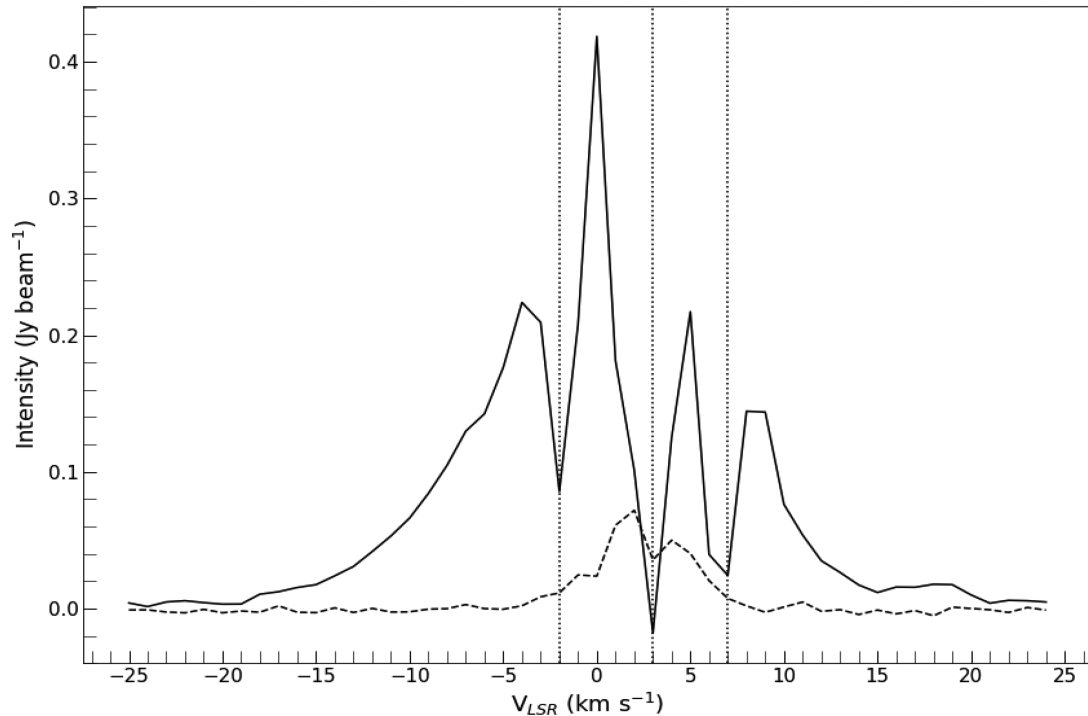
Figure 10. ^{12}CO (solid lines) and CH$_3$OH (dashed lines) spectra (of G188.95+0.89 extracted with an ellipse of size ~4 arcsec centred on MM2. The vertical lines indicate the observed absorption features in ^{12}CO line. The multiple absorption features in the ^{12}CO emission and the double peak feature in the CH$_3$OH line point to multiplicity (or at least binary) of driving sources in MM2. Band 7 ALMA dust continuum detected 2 cores in MM2.

(i) G188.95+0.89 protocluster is resolved into eight 1.3-mm objects (MM1-MM8). MM1 and MM2 are the central objects and MM1 (the brightest dust continuum object) is associated with the periodic 6.7-GHz CH$_3$OH maser source.

(ii) MM2 hosts more than one YSO, likely a binary system.

(iii) Strong emission of ^{12}CO at the east and west of MM2 point to the presence of an east–west bipolar outflow in MM2. Emissions north of MM2 also suggest a second outflow emanating from the object, which could signal multiplicity of YSOs in MM2.

(iv) All five features are periodic, suggesting a common background source of seed photon. The light curve shape of the maser features are similar to those of Mira variable stars and could suggest pulsation of the protostar as the possible driver of the periodicity (Inayoshi et al. 2013).

(v) Two CH$_3$OH maser features are reported with measurable velocity drift.

(vi) Outflows are identified in ^{12}CO (2-1) line emission. While no direct detection of accretion discs was possible with the current observations, the detected outflows suggest the presence of accretion discs in the source. Accretion disc may experience infalling gas and velocity drifts may be due to an artefact of variable line-merged features or by infalling gas.

DATA AVAILABILITY

(i) This paper makes use of the following ALMA data: ADS/JAO.ALMA 2015.101454.S. and can be accessed on the ALMA Science portal.

(ii) This publication makes use of data products HartRAO 26-m maser monitoring project and will be made available on a reasonable request.

(iii) The WISE data used in this publication can be access on the IRSA public data archive.

REFERENCES

Araya E. D., Hofner P., Goss W. M., Kurtz S., Richards A. M. S., Linz H., Olmi L., Sewiło M., 2010, ApJ, 717, L133
Breen S. L., Ellingsen S. P., Contreras Y., Green J. A., Caswell J. L., Stevens J. B., Dawson J. R., Voronkov M. A., 2013, MNRAS, 435, 524
Breen S. L., Sobolev A. M., Kaczmarek J. F., Ellingsen S. P., McCarthy T. P., Voronkov M. A., 2019, ApJ, 876, L25
Burns R. A. et al., 2020, Nature Astron, 4, 506
Caratti o Garatti A. et al., 2017, Nature Phys, 13, 276
Caswell J. L., 1996, MNRAS, 279, 79
Caswell J. L., Vaile R. A., Ellingsen S. P., 1995a, PASA, 12, 37
Caswell J. L., Vaile R. A., Ellingsen S. P., Whiteoak J. B., Norris R. P., 1995b, MNRAS, 272, 96
Durjasz M., Szymczak M., Wolak P., Bartkiewicz A., 2021, A&A, 648, A118

Fujisawa K. et al., 2014, PASJ, 66, 78

Fujisawa K., Yonekura Y., Sugiyama K., Horiuchi H., Hayashi T., Hachisuka K., Matsumoto N., Niinuma K., 2015, Astron. Telegram, 8286, 1

Gaylard M. J., 2010, MNRAS South Africa, 69, 168

Goddi C., Moscadelli L., Sanna A., 2011, A&A, 535, L8

Goedhart S., Gaylard M. J., van der Walt D. J., 2003, MNRAS, 339, L33

Goedhart S., Gaylard M. J., van der Walt D. J., 2004, MNRAS, 355, 553

Goedhart S., Langa M. C., Gaylard M. J., Van Der Walt D. J., 2009, MNRAS, 398, 995

Goedhart S., Maswanganye J. P., Gaylard M. J., van der Walt D. J., 2014, MNRAS, 437, 1808

Green J. A. et al., 2012, MNRAS, 420, 3108

Hildebrand R. H., 1983, QJRAS, 24, 267

Hu B., Menten K. M., Wu Y., Bartkiewicz A., Rygl K., Reid M. J., Urquhart J. S., Zheng X., 2016, ApJ, 833, 18

Hunter T. R. et al., 2017, ApJ, 837, L29

Hunter T. R., Brogan C. L., Chibueze J. O., Cyganowski C. J., Hirota T., MacLeod G. C., 2018, in Tarchi A., Reid M. J., Castangia P., eds, Proc. IAU Symp. 336, Astrophysical Masers: Unlocking the Mysteries of the Universe. Kluwer, Dordrecht, p. 251

Inayoshi K., Sugiyama K., Hosokawa T., Motogi K., Tanaka K. E. I., 2013, ApJ, 769, L20

Kurtz S., Cesaroni R., Churchwell E., Hofner P., Walmsley C. M., 2000, in Mannings V., Boss A. P., Russell S. S., eds, Protostars and Planets IV. Univ. Arizona Press, Tucson, AZ, p. 299

Lenz P., Breger M., 2004, in Zverko J., Ziznovsky J., Adelman S. J., Weiss W. W., eds, Proc. IAU Symp. 224, The A-Star Puzzle. Cambridge Univ. Press, Cambridge, p. 786

MacLeod G. C. et al., 2018, MNRAS, 478, 1077

MacLeod G. C. et al., 2019, MNRAS, 489, 3981

MacLeod G. C., Chibueze J. O., Sanna A., Paulsen J. D., Houde M., van den Heever S. P., Goedhart S., 2021a, MNRAS, 500, 3425

MacLeod G. C., Smits D. P., Green J. A., van den Heever S. P., 2021b, MNRAS, 502, 5658

Maswanganye J. P., Gaylard M. J., Goedhart S., Walt D. J. V. D., Booth R. S., 2015, MNRAS, 446, 2730

Maswanganye J. P., van der Walt D. J., Goedhart S., Gaylard M. J., 2016, MNRAS, 456, 4335

Menten K. M., 1991, ApJ, 380, L75

Minier V., Booth R. S., Conway J. E., 2000, A&A, 362, 1093

Minier V., Ellingsen S. P., Norris R. P., Booth R. S., 2003, A&A, 403, 1095

Minier V., Burton M. G., Hill T., Pestalozzi M. R., Purcell C. R., Garay G., Walsh A. J., Longmore S., 2005, A&A, 429, 945

Motte F., Bontemps S., Louvet F., 2018, ARA&A, 56, 41

Oh C. S., Kobayashi H., Honma M., Hirota T., Sato K., Ueno Y., 2010, PASJ, 62, 101

Olech M., Szymczak M., Wolak P., Gérard E., Bartkiewicz A., 2020, A&A, 634, A41

Ott M., Witzel A., Quirrenbach A., Krichbaum T. P., Standke K. J., Schalinski C. J., Hummel C. A., 1994, A&A, 284, 331

Proven-Adzri E., MacLeod G. C., Heever S. P. v. d., Hoare M. G., Kuditcher A., Goedhart S., 2019, MNRAS, 487, 2407

Reid M. J., Menten K. M., Brunthaler A., Zheng X. W., Moscadelli L., Xu Y., 2009, ApJ, 693, 397

Scargle J. D., 1982, ApJ, 263, 835

Sugiyama K. et al., 2015, Publ. Korean Astron. Soc., 30, 129

Sugiyama K. et al., 2017, PASJ, 69, 59

Sugiyama K., Saito Y., Yonekura Y., Momose M., 2019, Astron. Telegram, 12446, 1

Szymczak M., Hrynek G., Kus A. J., 2000, A&AS, 143, 269

Szymczak M., Wolak P., Bartkiewicz A., van Langevelde H. J., 2011, A&A, 531, L3

Szymczak M., Wolak P., Bartkiewicz A., 2014, MNRAS, 439, 407

Szymczak M., Wolak P., Bartkiewicz A., 2015, MNRAS, 448, 2284

Szymczak M., Olech M., Wolak P., Bartkiewicz A., Gawroński M., 2016, MNRAS, 459, L56

Szymczak M., Olech M., Sarniak R., Wolak P., Bartkiewicz A., 2018a, MNRAS, 474, 219

Szymczak M., Olech M., Wolak P., Gérard E., Bartkiewicz A., 2018b, A&A, 617, A80

Weingartner J. C., Draine B., 2001, ApJ, 548, 296

This paper has been typeset from a TeX/LaTeX file prepared by the author.